

Xing Wei · Rainer Hollerbach

Magnetic spherical Couette flow in linear combinations of axial and dipolar fields

Received: date / Accepted: date

Abstract We present axisymmetric numerical calculations of the fluid flow induced in a spherical shell with inner sphere rotating and outer sphere stationary. A magnetic field is also imposed, consisting of particular linear combinations of axial and dipolar fields, chosen to make $B_r = 0$ at either the outer sphere, or the inner, or in between. This leads to the formation of Shercliff shear layers at these particular locations. We then consider the effect of increasingly large inertial effects, and show that an outer Shercliff layer is eventually de-stabilized, an inner Shercliff layer appears to remain stable, and an in-between Shercliff layer is almost completely disrupted even before the onset of time-dependence, which does eventually occur though.

Keywords Spherical Couette flow · magnetohydrodynamics (MHD)

1 Introduction

Spherical Couette flow is the flow induced in a spherical shell by differentially rotating the inner and/or outer spheres. Magnetic spherical Couette flow, first considered by [1], is the magnetohydrodynamic analog, in which the fluid is taken to be electrically conducting, and a magnetic field is externally imposed. One motivation for studying this problem is to understand the dynamics of the Earth's molten iron outer core, and the magnetic field that is generated within it. There have also been two experiments on magnetic spherical Couette flow, the first in a uniform axial field imposed via Helmholtz coils from the outside [2], and the second in a dipolar field imposed via a permanent magnet embedded in the inner sphere [3,4].

The question of what type of field to impose is indeed fundamental in determining much of the subsequent dynamics. Even if we insist that this field be axisymmetric about the rotation axis of the inner and/or outer spheres (otherwise the problem immediately becomes fully three-dimensional), one could still impose an axial field from outside, or a dipole (or quadrupole) from inside, or indeed any combination of these. And because of the highly anisotropic nature of the magnetic tension force, coupling the fluid along the magnetic field lines, many of the results can be explained largely by the geometry of the imposed field. Fluid on field lines that thread only the inner or only the outer sphere will co-rotate with that sphere, whereas fluid on field lines linking the two spheres will rotate at some intermediate rate. The result is a shear layer, a so-called parallel or Shercliff layer, on the particular field line separating one type from another [5,6]. The thickness of these layers scales at $Ha^{-1/2}$, where the Hartmann number Ha is a measure of the strength of the imposed field.

Another issue that turns out to be surprisingly important concerns the nature of the inner and outer boundaries, and whether they are taken to be insulating or conducting. One obtains a standard Shercliff layer only if

Xing Wei
Institute of Geophysics, ETH, Zurich, 8092, Switzerland
E-mail: xing.wei@erdw.ethz.ch

Rainer Hollerbach
Department of Applied Mathematics, University of Leeds, Leeds, LS2 9JT, United Kingdom
E-mail: rh@maths.leeds.ac.uk

both spheres are insulating. For a conducting inner sphere, [7, 8, 9] showed that instead of merely a shear layer, one obtains a super-rotating region, in which fluid rotates slightly faster than either the inner or outer spheres. And finally, if both boundaries are conducting, this super-rotation can be made arbitrarily large, scaling as $O(Ha^{1/2})$ instead of $O(1)$ [10, 11]. These two types of super-rotation were both obtained for dipolar fields. For axial fields, one obtains a counter-rotation, which is again either $O(1)$ if only one boundary is conducting, or $O(Ha^{1/2})$ if both are [10, 12].

Motivated by these surprisingly different results for axial and dipolar fields, [13] considered linear combinations of the two, and showed that one may have super- and counter-rotating regions simultaneously. Furthermore, because axial and dipolar fields both have the same θ structure, differing only in r , one can adjust the particular linear combination so that the radial component of the field is zero on any desired radial shell. One can therefore choose the combination such that $B_r = 0$ on the outer sphere, or on the inner, or any radius in between. One can thereby precisely control the geometry of the imposed field: If $B_r = 0$ on the outer sphere, then all field lines thread only the inner sphere, and vice versa. If $B_r = 0$ at some intermediate radius, then some field lines thread only the inner sphere, and some only the outer. In no case though will there be any field lines linking the inner and outer spheres. In terms of the results discussed above, these particular linear combinations are therefore important special cases.

Having $B_r = 0$ on either the inner or outer boundary is also an important special case in terms of the structure of the Hartmann boundary layers that are generally expected to form there. It is known [14, 15] that the standard Hartmann layer breaks down at isolated points where $B_r = 0$, so if $B_r = 0$ everywhere on a particular boundary, the entire structure of the boundary layer there will be altered, becoming essentially a Shercliff layer that just happens to coincide with a boundary. It is for both of these reasons that these particular linear combinations of fields are worthy of special attention.

All of these special geometrical properties discussed so far are in the essentially linear regime, where the inertial term $\mathbf{U} \cdot \nabla \mathbf{U}$ is negligible, because the differential rotation between the two spheres is infinitesimal. It is obviously of interest then to consider what happens when this term is no longer negligible. At this point axial and dipolar fields again differ quite dramatically. For axial fields, the axisymmetric basic state is largely unaffected, and one is interested instead in the onset of non-axisymmetric instabilities [12, 16, 17]. In contrast, for dipolar fields, the basic state itself is strongly altered, with these particular field lines distinguishing one region from another becoming much less prominent [18].

In this work then we will essentially combine [13] and [18], taking the imposed fields to be these special linear combinations considered by [13], but extending this into the strongly nonlinear regime as in [18]. We will find the same general types of boundary layer instabilities as in [18], but will also show that having $B_r = 0$ at one boundary or the other, or in between, can still have a significant influence on the solutions.

2 Equations

The equations to be solved are essentially the same as in [12, 17],

$$\frac{\partial \mathbf{U}}{\partial t} + Re \mathbf{U} \cdot \nabla \mathbf{U} = -\nabla p + \nabla^2 \mathbf{U} + Ha^2 (\nabla \times \mathbf{b}) \times \mathbf{B}_0, \quad (1)$$

$$\mathbf{0} = \nabla^2 \mathbf{b} + \nabla \times (\mathbf{U} \times \mathbf{B}_0), \quad (2)$$

except that \mathbf{B}_0 will no longer be a purely axial field.

Length is scaled by the radius of the inner sphere r_i , time by the viscous diffusive timescale r_i^2/ν , where ν is the viscosity. \mathbf{U} is scaled by Ωr_i , where Ω is the imposed rotation rate of the inner sphere (with a stationary outer sphere). The Reynolds number $Re = \Omega r_i^2/\nu$ is then the non-dimensional measure of Ω . The Hartmann number $Ha = B_0 r_i / \sqrt{\mu \rho \nu \eta}$ similarly measures the strength of the imposed field B_0 , where μ , ρ , and η are respectively the permeability, density, and magnetic diffusivity.

These equations have been formulated in the limit of infinitesimal magnetic Reynolds number $Rm = \Omega r_i^2/\eta$, in which the induced magnetic field is given by $Rm \mathbf{b}$, but Rm no longer appears in the actual equations to be solved. In this $Rm \rightarrow 0$ limit the Lorentz force $(\nabla \times \mathbf{b}) \times \mathbf{B}_0$ in (1), and the inductive term $\nabla \times (\mathbf{U} \times \mathbf{B}_0)$ in (2) also become linear. The only nonlinearity is therefore the inertial term $Re \mathbf{U} \cdot \nabla \mathbf{U}$.

The boundary conditions associated with (1) are

$$\mathbf{U} = \sin \theta \hat{\mathbf{e}}_\phi \quad \text{at} \quad r = r_i, \quad \mathbf{U} = \mathbf{0} \quad \text{at} \quad r = r_o, \quad (3)$$

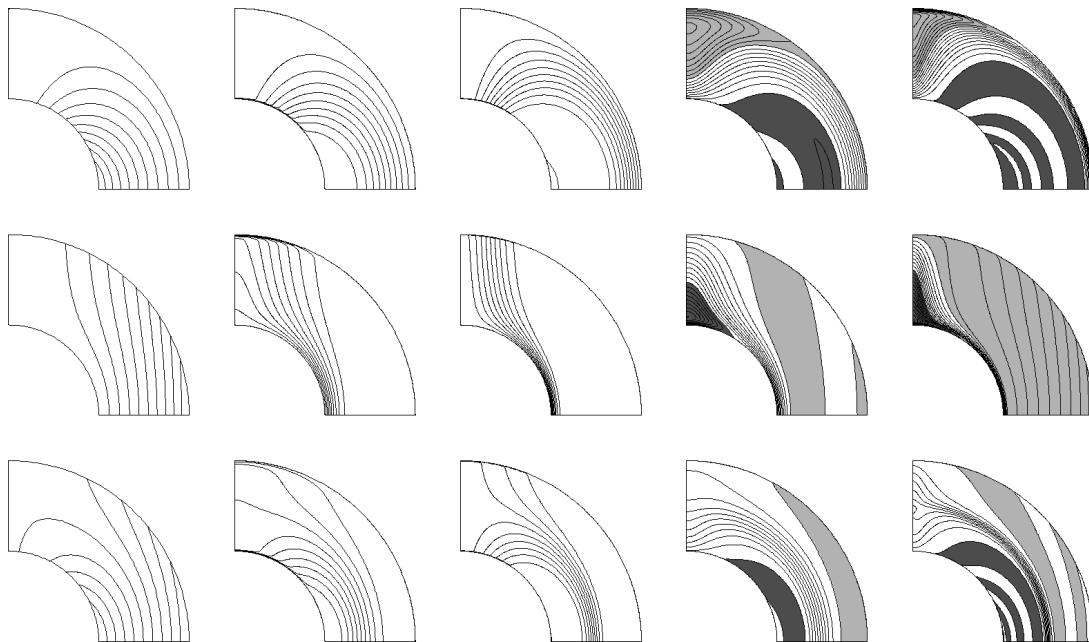


Fig. 1 From top to bottom, the three rows are at $\varepsilon = -1, -8,$ and $-8/1.5^3$. The first panel in each row shows the field lines of the corresponding imposed fields \mathbf{B}_0 ; note in particular how $B_r = 0$ at $r = 2, 1,$ and $1.5,$ respectively. The next four panels show contours of the angular velocity ω , with a contour interval 0.1, for the four cases ($Ha = 10^2, \text{II}$), ($Ha = 10^3, \text{II}$), ($Ha = 10^2, \text{CC}$), ($Ha = 10^3, \text{CC}$), and all at $Re = 0$. For the CC results, dark-shaded regions are super-rotating ($\omega > 1$), and light-shaded regions are counter-rotating ($\omega < 0$).

where we fix $r_i = 1$ and $r_o = 2$. The boundary conditions associated with (2) are somewhat more complicated, and in particular depend on whether the inner and outer regions are taken to be insulators or conductors. There are then four possible combinations, II, CI, IC, and CC, where the first letter indicates the inner boundary and the second letter the outer. We will present only II and CC results here; the other two cases do not appear to yield fundamentally new dynamics. See [10] for sample calculations of all four, but only in the linear limit $Re \rightarrow 0$. For the actual mathematical formulation of the II and CC boundary conditions, we refer to [12], where both are derived in detail.

These equations and associated boundary conditions are solved using the code described by [19], in which the radial structure is expanded in terms of Chebyshev polynomials, and the angular structure in terms of spherical harmonics. In this work we will consider only axisymmetric solutions, so the code was reduced to a two-dimensional version, with no variation in ϕ . In r and θ , resolutions as high as 150 and 700 respectively were used. Equation (1) is time-stepped by a second-order Runge-Kutta method, modified to treat the diffusive term implicitly. At each time-step of (1), (2) is inverted for \mathbf{b} .

The imposed field \mathbf{B}_0 is taken to be a linear combination of dipolar and axial fields,

$$\mathbf{B}_0 = C(\mathbf{B}_d + \varepsilon\mathbf{B}_a), \quad \text{where} \quad \mathbf{B}_d = 8r^{-3} \cos \theta \hat{\mathbf{e}}_r + 4r^{-3} \sin \theta \hat{\mathbf{e}}_\theta, \quad \mathbf{B}_a = \cos \theta \hat{\mathbf{e}}_r - \sin \theta \hat{\mathbf{e}}_\theta. \quad (4)$$

Note how \mathbf{B}_d and \mathbf{B}_a have the same θ dependence; by adjusting ε one can therefore impose $B_r = 0$ on the particular radial surface $r = -2/\varepsilon^{1/3}$. We will consider $\varepsilon = -1, -8,$ and $-8/1.5^3$, yielding $B_r = 0$ on the outer boundary, the inner boundary, and at the midpoint $r = 1.5$. Finally, once ε has been specified, the constant C is adjusted such that the volume-averaged field strength is unity, $\int_V |\mathbf{B}_0|^2 dV/V = 1$. Its dimensional magnitude has after all already been incorporated into the Hartmann number. The field still has considerable spatial variation though, so Hartmann numbers for different ε are not necessarily directly comparable.

3 Results

We begin by reviewing the $Re \rightarrow 0$ linear regime previously considered by [10, 13]. Figure 1 shows both the imposed fields \mathbf{B}_0 , as well as the resulting angular velocities. Focusing first on the simpler II cases, we see

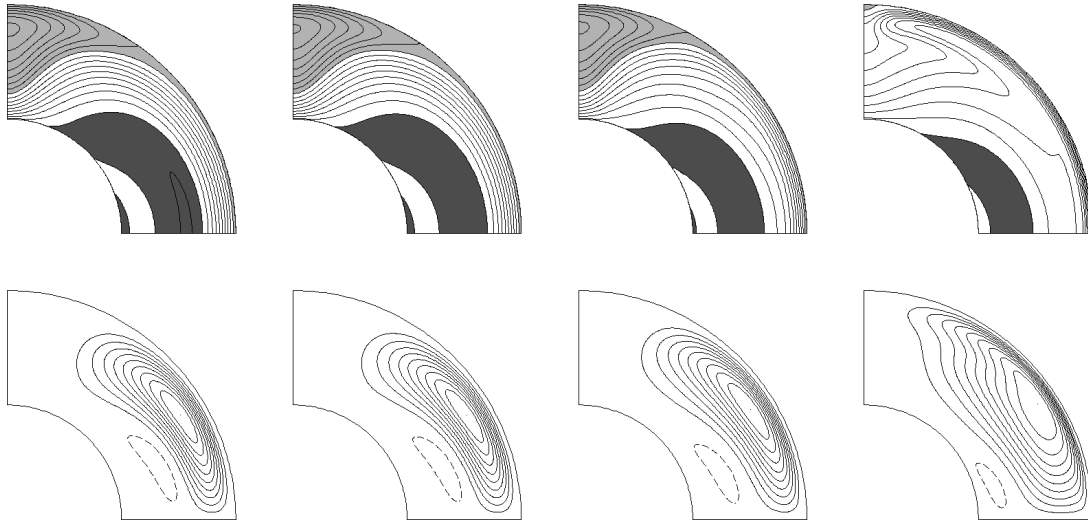


Fig. 2 The $\varepsilon = -1$, CC solutions, for $Ha = 10^2$, and $Re = 30, 100, 300$, and 1000 , from left to right. The top row shows contours of the angular velocity, as in Figure 1. The bottom row shows streamlines of the meridional circulation ψ , with solid lines denoting counter-clockwise flow, and dashed lines clockwise. From left to right, the maximum values of ψ are 7.26×10^{-3} , 2.33×10^{-2} , 5.14×10^{-2} , and 5.13×10^{-2} .

that the angular velocity ω is essentially constant on field lines of \mathbf{B}_0 , as expected according to Ferraro's law of isorotation [20]. A Shercliff layer forms at the radius where $B_r = 0$. Hartmann layers also form at boundaries where $B_r \neq 0$. The Hartmann layers are much thinner than the Shercliff layers, scaling as Ha^{-1} versus $Ha^{-1/2}$.

Turning next to the CC cases, we see that there are now regions that are super-rotating, with $\omega > 1$, as well as counter-rotating, with $\omega < 0$. With conducting boundaries, electric currents can recirculate through them, leading to increased currents in the fluid, and hence increased Lorentz forces, which accelerate the fluid into super- and counter-rotation. The Shercliff layers are in the same locations as in the II cases, but are considerably thinner than before (but still scale as $Ha^{-1/2}$). The Hartmann layers have been largely eliminated; the electro-magnetic coupling across a conducting boundary is so strong that such boundary layers cannot exist as before.

A few calculations were also done for CI and IC boundary conditions, with the following results: For $\varepsilon = -1$, CI is similar to CC, and IC is similar to II, whereas for $\varepsilon = -8$, CI is similar to II, and IC is similar to CC. The classification is evidently determined by the boundary where $B_r \neq 0$, that is, by the boundary where a Hartmann layer forms for I, but is suppressed for C. In contrast, Shercliff layers can form at both I and C boundaries (because they are not really boundary layers at all, but rather internal shear layers that just happen to coincide with the boundaries for the special cases $\varepsilon = -1$ and -8). It is not surprising then that the boundary where $B_r \neq 0$ is more important in determining the similarities between different cases.

In the remainder of this paper we wish to consider the influence of increasingly large Re on these solutions in Figure 1. Figure 2 shows the $\varepsilon = -1$, CC results, for $Ha = 10^2$ and Re from 30 to 1000. One new feature that immediately emerges as soon as $Re > 0$ is a meridional circulation. This acts back on the angular velocity in a number of ways. First, because it is outward near the equator, it tends to compress the Shercliff layer against the outer boundary, so that by $Re = 1000$ it is much thinner than it was for $Re = 0$. Second, we note that by $Re = 1000$ the counter-rotation has been almost completely eliminated, and the super-rotation has also been considerably reduced.

In Figure 3, Re is further increased to 3000, which results in a time-dependent solution. The time-dependence is almost exclusively confined to the Shercliff layer though, consisting of a series of ripples within this layer. It is quite similar to the time-dependent solutions previously obtained in a purely dipolar field [18], even though the boundary layer in that case was a true Hartmann layer rather than the Shercliff layer here. For $Re > 0$ the distinction between Hartmann and Shercliff layers is apparently less critical than it is for $Re = 0$.

For $Ha = 10^2$, the onset of this time-dependence is at $Re_c \approx 2200$, and appears to be a subcritical Hopf bifurcation. That is, if one gradually increases Re until the onset of instabilities, and then decreases it again,

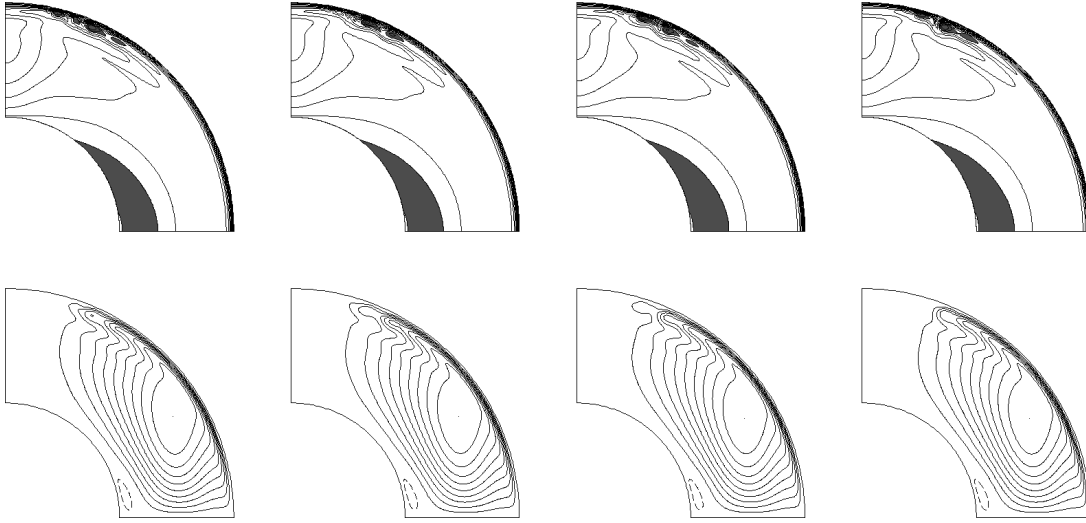


Fig. 3 The $\varepsilon = -1$, CC solution, for $Ha = 10^2$ and $Re = 3000$. From left to right, four snapshots of the time-dependent solution, uniformly spaced throughout the period $\tau = 27$. As in Figure 2, the top row shows contours of ω , the bottom row ψ , with $\psi_{max} = 3.56 \times 10^{-2}$.

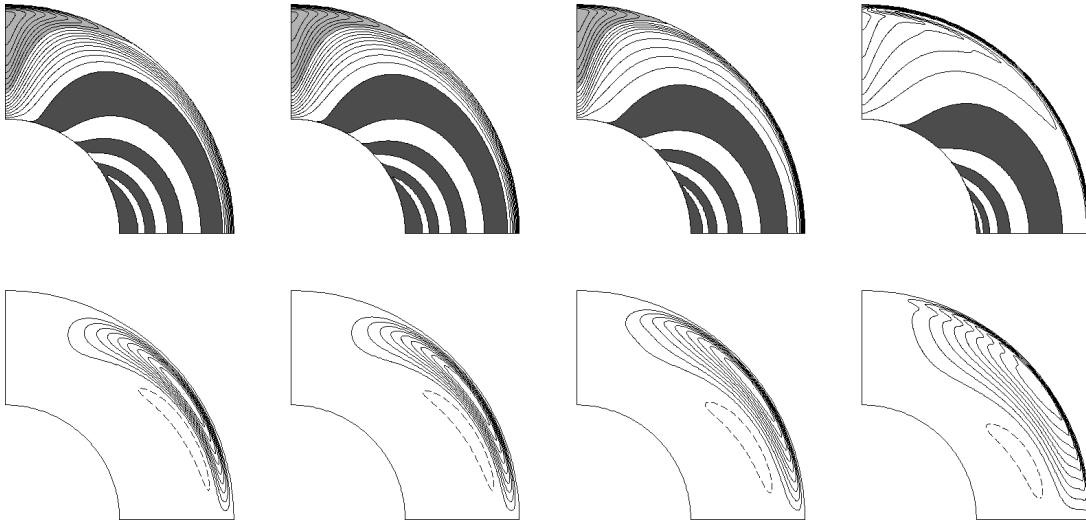


Fig. 4 The $\varepsilon = -1$, CC solutions, for $Ha = 10^3$, and $Re = 300, 1000, 3000, 10000$, from left to right. As in Figure 2, the top row shows contours of ω , the bottom row ψ , with $\psi_{max} = 4.17 \times 10^{-3}, 1.27 \times 10^{-2}, 2.18 \times 10^{-2}$, and 1.72×10^{-2} .

there is a certain degree of hysteresis before one switches back to the steady solutions. These calculations are unfortunately too time-consuming to allow a precise determination of the initial Re_c , or the extent of the hysteresis.

If we next increase the Hartmann number to $Ha = 10^{2.5}$, the onset of time-dependence is at $Re_c \approx 6000$ (again with hysteresis), perhaps suggesting an $Re_c \sim Ha$ scaling. Precisely determining how Re_c scales with Ha would obviously be even more time-consuming though than simply determining it at any particular value of Ha . Further increasing Ha to 10^3 , the solutions are (not surprisingly) stable at least up to $Re = 10000$. Figure 4 shows results for $Ha = 10^3$ and Re from 300 to 10000. One very interesting result emerges from comparing the two $Re = 1000$ solutions in Figures 2 and 4: the thickness of the Shercliff layer now appears to be controlled far more by Re than by Ha . There are unfortunately no analytic predictions to compare with in this nonlinear regime.

Figure 5 shows the result of switching from CC to II boundary conditions. We still obtain a time-dependence very similar to that in Figure 3, but the onset does not occur until $Re_c \approx 6500$, again with hysteresis. II boundaries are therefore considerably more stable than CC. The reason for this is straightforward: For CC, the

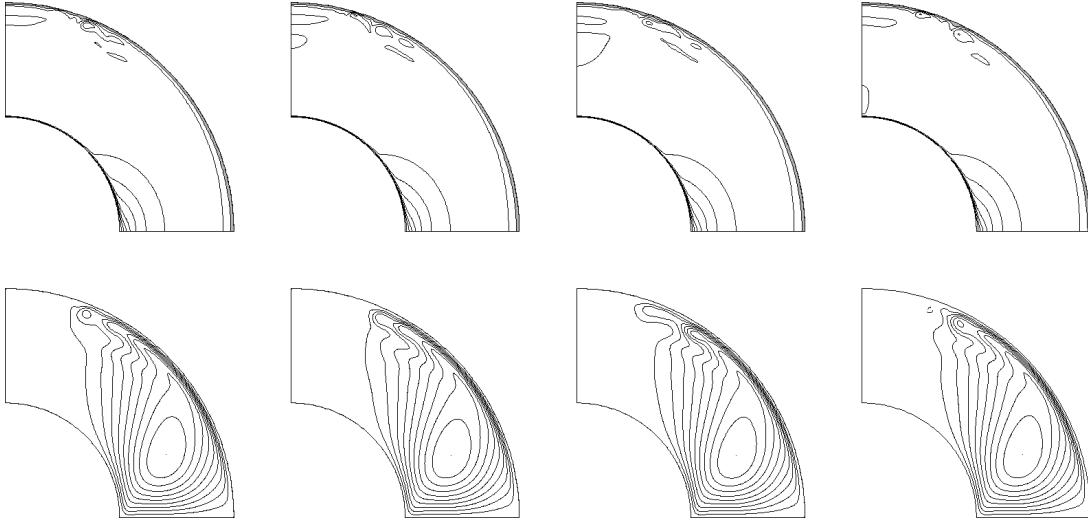


Fig. 5 The $\varepsilon = -1$, II solution, for $Ha = 10^2$ and $Re = 10000$. From left to right, four snapshots of the time-dependent solution, uniformly spaced throughout the period $\tau = 20$. As in Figure 2, the top row shows contours of ω , the bottom row ψ , with $\psi_{max} = 1.31 \times 10^{-2}$.

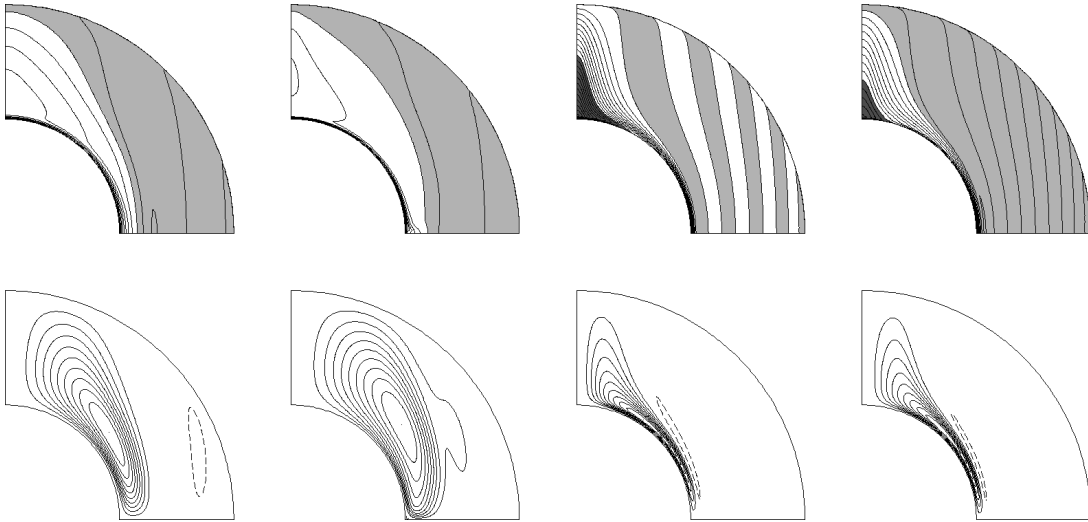


Fig. 6 The $\varepsilon = -8$, CC solutions, from left to right ($Ha = 10^2$, $Re = 3000$), ($Ha = 10^2$, $Re = 10000$), ($Ha = 10^3$, $Re = 3000$), ($Ha = 10^3$, $Re = 10000$). As in Figure 2, the top row shows contours of ω , the bottom row ψ , with $\psi_{max} = 1.40 \times 10^{-2}$, 1.24×10^{-2} , 1.26×10^{-3} , and 2.93×10^{-3} .

Hartmann layer on the inner boundary is completely suppressed, so all of the adjustment in angular velocity occurs across the Shercliff layer at the outer boundary. In contrast, for II, much of the adjustment occurs across the Hartmann layer, so the Shercliff layer is considerably weaker than for CC. A weaker Shercliff layer then requires a much larger Reynolds number before it will become unstable.

We next switch to $\varepsilon = -8$. Figure 6 shows these solutions, at $Ha = 10^2$ and 10^3 , and $Re = 3000$ and 10000 for each. Increasing Ha again increases the super-/counter-rotation, whereas increasing Re suppresses them. In this case the inner Shercliff layer is very stable though, with no evidence of any transition to time-dependence even up to $Re = 30000$. Partly this may be due to the spatial variation of \mathbf{B}_0 ; B_θ at the inner boundary for $\varepsilon = -8$ is $8\sqrt{5/68} = 2.2$ times stronger than B_θ at the outer boundary for $\varepsilon = -1$. It seems very unlikely though that a mere 2.2 times increase in field strength (for a given Hartmann number) could by itself cause such an enormous increase in critical Reynolds number, from ~ 2200 to over 30000 . We conclude therefore that an inner Shercliff layer is intrinsically more stable than an outer Shercliff layer. The instabilities

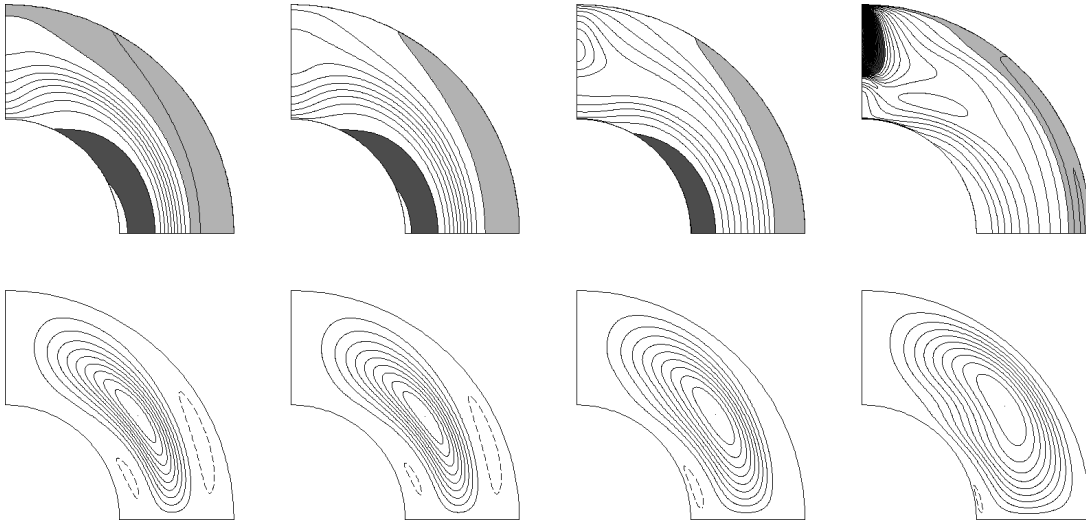


Fig. 7 The $\varepsilon = -8/1.5^3$, CC solutions, for $Ha = 10^2$, and $Re = 100, 300, 1000, 3000$, from left to right. As in Figure 2, the top row shows contours of ω , the bottom row ψ , with $\psi_{max} = 7.71 \times 10^{-3}, 2.15 \times 10^{-2}, 4.55 \times 10^{-2}$, and 6.64×10^{-2} .

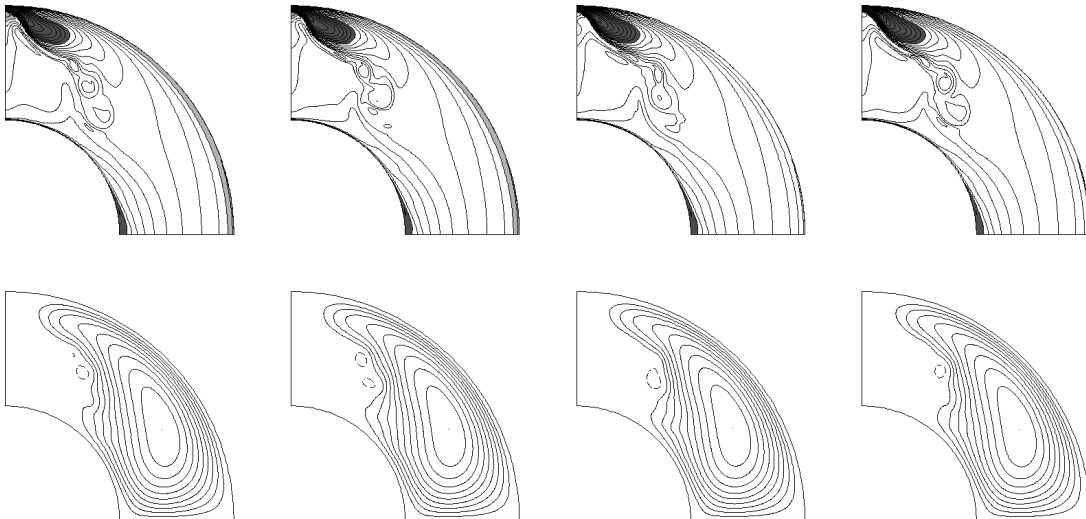


Fig. 8 The $\varepsilon = -8/1.5^3$, CC solution, for $Ha = 10^2$ and $Re = 10000$. From left to right, four snapshots of the time-dependent solution, uniformly spaced throughout the period $\tau = 10$. As in Figure 2, the top row shows contours of ω , the bottom row ψ , with $\psi_{max} = 7.44 \times 10^{-2}$.

of the outer Shercliff layer are perhaps similar to Görtler vortices, which also occur only if a boundary is curved one way, but not the other.

Finally, Figures 7 and 8 show results for $\varepsilon = -8/1.5^3$. Increasing Re in this case appears to destroy the Shercliff layer completely. For sufficiently large Re these solutions again become time-dependent, but the instabilities are no longer confined to boundary layers. One further new feature that emerges for sufficiently large Re is a super-rotating region near the pole. This is quite different from the previous super-rotations though, which were all driven by the Lorentz force. In contrast, this super-rotation is induced by the inertial term: as the meridional circulation sweeps fluid inward toward the pole, conservation of angular momentum causes its angular velocity to increase, eventually exceeding one.

4 Conclusion

In this work we have considered magnetic spherical Couette flow in three particular field configurations \mathbf{B}_0 , specifically chosen to place Shercliff layers at either the outer boundary, or the inner, or exactly in between. In each case we then increased the Reynolds number, and studied the resulting balance and competition between magnetic and inertial effects. We found that increasing the Hartmann number stabilizes the solutions, whereas increasing the Reynolds number tends to de-stabilize them, except for $\varepsilon = -8$, where we never obtained any instabilities. It would be of interest to further increase Re in this case; some type of instabilities must surely set in eventually, but not necessarily boundary layer instabilities of the type obtained for $\varepsilon = -1$. Future work should also explore the possibility of non-axisymmetric instabilities, as in the purely axial field case [12, 16, 17].

Finally, returning to the magnetic spherical Couette flow experiments that have previously been done [2, 3, 4], it would be of considerable interest to extend one or the other of these to impose not just purely axial or purely dipolar fields, but some of the configurations presented here. We hope our results may stimulate future experimental work in this direction.

Acknowledgements We thank Prof. Andrew Jackson for providing the computational facilities.

References

1. Hollerbach, R.: Magnetohydrodynamic Ekman and Stewartson layers in a rotating spherical shell. *Proc. R. Soc. Lond. A* **444**, 333–346 (1994).
2. Sisan, D.R., Mujica, N., Tillotson, W.A., Huang, Y.M., Dorland, W., Hassam, A.B., Antonsen, T.M., Lathrop, D.P.: Experimental observation and characterization of the magnetorotational instability. *Phys. Rev. Lett.* **93**, 114502 (2004).
3. Nataf, H.-C., Alboussiere, T., Brito, D., Cardin, P., Gagniere, N., Jault, D., Masson, J.-P., Schmitt, D.: Experimental study of super-rotation in a magnetostrophic spherical Couette flow. *Geophys. Astrophys. Fluid Dynam.* **100**, 281–298 (2006).
4. Schmitt, D., Alboussiere, T., Brito, D., Cardin, P., Gagniere, N., Jault, D., Nataf, H.-C.: Rotating spherical Couette flow in a dipolar magnetic field: experimental study of magneto-inertial waves. *J. Fluid Mech.* **604**, 175–197 (2008).
5. Starchenko, S.V.: Magnetohydrodynamics of a viscous spherical layer rotating in a strong potential field. *J. Exper. Theor. Phys.* **85**, 1125–1137 (1997).
6. Starchenko, S.V.: Magnetohydrodynamic flow between insulating shells rotating in strong potential field. *Phys. Fluids* **10**, 2412–2420 (1998).
7. Dormy, E., Cardin, P., Jault, D.: MHD flow in a slightly differentially rotating spherical shell with conducting inner core in a dipolar magnetic field. *Earth Planet. Sci. Lett.* **160**, 15–30 (1998).
8. Dormy, E., Jault, D., Soward, A.M.: A super-rotating shear layer in magnetohydrodynamic spherical Couette flow. *J. Fluid Mech.* **452**, 263–291 (2002).
9. Mizerski, K.A., Bajer, K.: On the effect of mantle conductivity on the super-rotating jets near the liquid core surface. *Phys. Earth Planet. Inter.* **160**, 245–268 (2007).
10. Hollerbach, R.: Magnetohydrodynamic flows in spherical shells. In: Egbers, C., Pfister, G. (eds), *Physics of Rotating Fluids. Lecture Notes in Physics* **549**, Springer, 295–316 (2000).
11. Buehler, L.: On the origin of super-rotating tangential layer in magnetohydrodynamic flows. <http://bibliothek.fzk.de/zb/berichte/FZKA7028.pdf> (2004).
12. Hollerbach, R., Skinner, S.: Instabilities of magnetically induced shear layers and jets. *Proc. R. Soc. Lond. A* **457**, 785–802 (2001).
13. Hollerbach, R.: Super- and counter-rotating jets and vortices in strongly magnetic spherical Couette flow. In: Chossat, P., Arbruster, D., Oprea, J. (eds), *Dynamo and Dynamics, a Mathematical Challenge. NATO Science Series II* **26**, Dordrecht, 189–197 (2001).
14. Roberts, P.H.: Singularities of Hartmann layers. *Proc. R. Soc. Lond. A* **300**, 94–107 (1967).
15. Loper, D.E.: General solution for the linearised Ekman-Hartmann layer on a spherical boundary. *Phys. Fluids* **12**, 2995–2998 (1970).
16. Wei, X., Hollerbach, R.: Instabilities of Shercliff and Stewartson layers in spherical Couette flow. *Phys. Rev. E* **78**, 026309 (2008).
17. Hollerbach, R.: Non-axisymmetric instabilities in magnetic spherical Couette flow. *Proc. R. Soc. Lond. A* **465**, 2003–2013 (2009).
18. Hollerbach, R., Canet, E., Fournier, A.: Spherical Couette flow in a dipolar magnetic field. *Eur. J. Mech. B* **26**, 729–737 (2007).
19. Hollerbach, R.: A spectral solution of the magneto-convection equations in spherical geometry. *Int. J. Numer. Meth. Fluids* **32**, 773–797 (2000).
20. Cowling, T.G.: *Magnetohydrodynamics*. Interscience, New York (1957).